University of Tartu

Faculty of Science and Technology

Institute of Technology

Joosep Kivastik

Optical Design of a Radiometrically Calibrated Miniature Earth Observation Imager

Master's Thesis (30 ECTS)
Robotics and Computer Engineering Curriculum

Supervisors:

Hendrik Ehrpais, MSc
Nikolay Voznesenskiy, Dr.Sci.

Tartu 2019

Abstract

Optical Design of a Radiometrically Calibrated Miniature Earth Observation Imager

In this thesis a diffraction limited optical design for a radiometrically calibrated miniature multispectral Earth observation imager is proposed and its performance analysed. The goal of the imager is to capture quantitative data for remote sensing with a radiometric accuracy of 5% during a three year lifetime in Low Earth Orbit. The design is based on optical and radiometric requirements that were derived from a radiometric budget analysis and the requirements from the original proposal. The budget also set requirements for different optical components which were chosen as part of this work. A tolerance analysis was performed on the optical design taking into account the uncertainties from manufacturing and assembly. It was found that instrument design fulfills the original requirements and it will be used to build a prototype instrument for the European Space Agency.

CERCS: P200 Electromagnetism, optics, acoustics; T110 Instrumentation technology; T320 Space Technology

Keywords: imager, remote sensing, optics, instrument design, radiometry, tolerancing

Radiomeetriliselt kalibreeritud miniatuurse maavaatluskaamera optiline ülesehitus

Magistritöö raames töötati välja radiomeetriliselt kalibreeritud miniatuurse multispektraalse maavaatluskaamera difratksiooniga piiratud optiline ülesehitus ning viidi läbi selle kvaliteedi analüüs. Kaamera eesmärk on kolmeaastase eluea vältel Maa-lähedasel orbiidil jäädvustada kvantitatiivseid kaugseire andmeid, mille radiomeetriline täpsus on 5%. Kaamera optiline ülesehitus põhineb optilistel ja radiomeetrilistel nõuetel, mis tulenevad projekti esialgsest kirjeldusest ning radiomeetrilise eelarve analüüsist. Eelarve tingis nõuded ka teistele optika komponentidele, mis valiti välja selle töö käigus. Optilisele disainile tehti ka tolerantsianalüüs, mis põhines kaamera valmistamisel ning kokkupanekul tekkivatel määramatustel. Analüüs näitas, et kaamera disain vastab algupärastele nõuetele ning sellest lähtuvalt ehitatakse prototüüp Euroopa Kosmoseagentuuri jaoks.

CERCS: P200 Elektromagnetism, optika, akustika; T110 Instrumentatsioonitehnoloogia; T320 Kosmosetehnoloogia

Märksõnad: kaamera, kaugseire, optika, instrumendi disain, radiomeetria, tolerantsianalüüs

Contents

List of Figures

List of Tables

Acronyms and Abbreviations

1U - One Unit

AR - Anti-Reflection

BFL - Back Focal Length

BSI - Backside Illuminated

CCD - Charge-Coupled Device

CMOS - Complementary Metal-Oxide-Semiconductor

CWL - Central Wavelength

EOI - Earth Observation Imager

ESA - European Space Agency

F# - F-number

FWHM - Full Width at Half Maximum

FOV - Field of View

FWC - Full Well Capacity

GSD - Ground Sampling Distance

MTF - Modulation Transfer Function

NIR - Near-Infrared

NDVI - Normalised Difference Vegetation Index

QE - Quantum Efficiency

RMS - Root Mean Square

SAG - Sagitta

sCMOS - Scientific Complementary Metal-Oxide-Semiconductor

SFE - Surface Form Error

SNR - Signal-to-Noise Ratio

TOA - Top of Atmopshere

1 Introduction

Space is becoming more affordable and accessible. Each year an increasing number of standardised nanosatellites (CubeSats [1]) are being launched into orbit. [2] Nearly all of these satellites are either experimental CubeSats built by student teams (AAUSAT-II [3], ALLSTAR-1 [4], ESTCube-1 [5] etc.) from different universities, or by companies such as Planet Labs, which launch large Earth observation constellations [6]. Most of these nanosatellites have imagers on-board, either for publicity or to provide high temporal frequency imagery of the Earth. However, almost all of these cameras are meant to capture visually good looking images without putting any particular emphasis on their radiometric accuracy. There are some examples of calibrated imagers. For example the HyperScout by Cosine [7], which is a hyperspectral imager that has a 5% radiometric accuracy requirement, but no information was available, if that accuracy was achieved. Furthermore, if the accuracy is available, then due to the lack of an on-board calibration system it is questionable if the accuracy can be preserved. It is possible to use vicarious calibration methods by imaging known landmarks, but an on-board system gives the instrument more properties to calibrate.

1.1 Problem Overview

Having a constellation of CubeSats with radiometrically accurate imagers would make high temporal frequency quantitative remote sensing possible. This is needed for monitoring the land cover change [8], agricultural management [9], vegetetation phenology [10], and etc. better. This would be advantageous on nanosatellites for many reasons. For example, compared to a ”Landsat-class” Earth observation satellites, the cost of designing, manufacturing and launching a single nanosatellite is a few orders of magnitude smaller [11] [12] [13]. Of course it is not possible to achieve the same kind of quality - the accuracy and resolution would both be worse, but not significantly, which makes it possible for these CubeSats to provide complimentary data for bigger satellites. Secondly, due to the low cost it is possible to iterate on the satellites faster. For example, one can launch 10 - 20 satellites into orbit, do a lessons learned, iterate, and send a new batch - this all within a fraction of Sentinel-2’s monetary and temporal budget. Thirdly, again due to the low cost it is possible to put the satellites in lower and more hazardous orbits that would be too dangerous for high-cost satellites. Finally, having a constellation of such satellites it is also possible to study the angular distribution of a target’s reflectance by having multiple satellites study the same area simultaneously. These are the reasons why Tartu Observatory is developing a radiometrically calibrated miniature multispectral Earth observation imager (hereinafter Theia) in cooperation with ESA under the Industry Incetive Scheme. The EOI is meant as a companion piece to Sentinel-2 [14]. Currently the project design phase has ended and testing of the imager should begin by the Autumn of 2019.

1.2 Thesis Goals

This thesis has two main goals: an optical design of the imager and developing its radiometric budget. These two can be further divided into the following objectives:

- define the optical and radiometrical requirements,
- optical design and analysis,
- component selection,
- radiometric budget analysis,
- tolerancing analysis.

2 Theoretical Framework

In this chapter I will give an overview of the terminology used in the thesis. This will cover optics, sensors, and remote sensing.

2.1 Optics

Aperture stop in an optical system limits the size of an axial cone of energy from the object. All other elements of the system can accept a bigger cone. [15]

Chief ray is a ray from an off-axis object point which passes through the center of the aperture stop of the optical system. [16]

Telecentricity is a property of an optical system in which the chief rays are collimated and parallel to the optical axis in image and/or object space. [17]

Airy disk is the diffraction pattern of a circular aperture that establishes the limit to the optical performance which can be expected from an optical device. [15] The diameter can be calculated as

$$D[\mu m] = 2.44\lambda[\mu m]F\#, \tag{2.1}$$

where λ is the wavelength. [18]

Optical aberrations are deviations from a perfect mathematical model. These can be caused either by the optical elements' shapes, placements, or due to the wave nature of light. [19]

Sag is the displacement of the optical element's curve along the optical axis from the optical element vertex. [20]

Conic constant - is the negative square of the eccentricity of an elliptical surface, defined by the equation

$$k = -\epsilon^2 = -\frac{a^2 - b^2}{a^2}, \tag{2.2}$$

where

- ϵ - eccentricity,
- a - semi-major axis length,
- b - semi-minor axis length.

Depending on the value of k, the optical element surface can either be one of the following conical sections:

- $k > 0$ - oblate ellispoid,
- $k = 0$ - sphere,
- $0 > k > -1$ - parabola,
- $k < -1$ - hyperbola. [20]

Aspherical element is an optical element where the surface sag is defined by the equation:

$$z = \frac{cr^2}{1 + \sqrt{1 - c^2(k+1)r^2}} + \alpha_1 r^4 + \alpha_2 r^6 + \alpha_3 r^8 + \alpha_4 r^{10}, \tag{2.3}$$

where

- c - curvature,
- r - aperture radius,
- k - conic constant,
- $\alpha_{1..4}$ are higher order aspheric coefficients. [20]

Freeform surface is a surface that has no translational or rotational symmetries about axes normal to the mean plane. The surface's sag is usually defined by a polynomial. [21]

Diffraction-limited system is when geometrically all the rays fall inside the Airy disk of the imaging system and therefore, the system resolution is limited by the wave nature of light. [15]

PSF is the impulse response function of a point source. This is considered to be one of the fundamental units in image formation models. [20] [22]

Modulation Transfer Function is the modulus of the optical transfer function which is the Fourier transform of the PSF. The MTF shows the ratio of the modulation in the image to the modulation in the object, which is also known as contrast of a specific resolution. Resolution here is defined as either tangetial or sagittal black and white lines per millimeter. [20] [23]

Strehl ratio - Ratio of the peak value of the PSF to the peak of the PSF for an equivalent perfect (unaberrated) system. A system is said to be diffraction limited if the Strehl ratio is bigger than 0.8. [20]

WFE is the deviation from a perfect wavefront. According to the Marechal approximation the WFE is related to the Strehl ratio as:

$$S = e^{-(\frac{2\pi\sigma}{\lambda})^2}, \tag{2.4}$$

- λ - wavelength,
- σ - WFE. [20]

Marechal criterion says that a system is diffraction limited, if RMS WFE $< 0.07\lambda$.

Zernike polynomials are a complete set of polynomials that are orthogonal over the interior of the unit circle. The terminology, normalization, and notation used for Zernike polynomials is not uniform. The polynomials are used to represent wavefront data, because the different Zernike polynomials correspond to different optical aberrations also seen in optical tests. [20] [24]

2.2 Sensor

sCMOS is a new type of CMOS image sensor that has low noise and high dynamic range at the same time. This was achieved with a novel 6 transistor pixel architecture. More can be read at [25].

Quantum efficiency is the ratio of light incident on the sensor to the amount that gets converted into electrons. QE is wavelength dependent. [26]

Pixel pitch denotes the physical size of the pixel, usually in μm.

Shot noise is a source of noise that is inherently physical. It says that the distribution of photons fluctuates according to the Poisson distribution, which means that the variance of the electrons is

$$\sigma_e = \sqrt{\mu_e}, \tag{2.5}$$

where μ_e is the mean number of electrons. [26]

2.3 Remote Sensing

Spectral band is a region of the optical spectrum usually defined by its central wavelength and its band thickness, mostly by denoting its full width at half maximum. In this thesis the bands are written as CWL(FWHM).

Normalised Difference Vegetation Index is a remote sensing index that indicates the density of green leaves in the imaged area based on the fact that chlorophyll strongly absorbs visible light (from 0.4 μm to 0.7 μm) and the cell structure of the leaves strongly reflects near-infrared light (from 0.7 μm to 1.1 μm). Thus the more leaves the plant has the more it reflects and the greener it is the more it absorbs. The index is given by the ratio

$$NDVI = \frac{NIR - VIS}{NIR + VIS}, \tag{2.6}$$

where VIS denotes the reflected light of a spectral band between 0.4 μm and 0.7 μm. [27]

Top of atmosphere radiance is the radiance measured by remote sensing instruments. This includes the radiation reflected from Earth's surface, the imager's internal structure, and the

radiation reflected directly from the clouds. [28]

3 Application

In this chapter the foundation, from which the design is derived, is shown.

3.1 Idea

The concept of the imager is that it can be integrated into various different nanosatellites. A specific type of small satellites is defined by the CubeSat standard [1], which is a convenient way to define an instrument so that the ease of integration for the user is increased. For this reason it was chosen that the instrument will comply with the standard. Moreover, as an extra miniaturisation step it was also decided to have it fit within the one unit size of less than 10x10x10 (cm). Furthermore, modularity was kept in mind during the design process to make assembly, integration, testing easier, and this also makes it possible to change the spectral bands without redesigning the imager possible. To be able to fly on different satellites interfacability is key, this is why Theia will support various communication protocols and will have simple to adapt mechanics. The main idea is that the imager will be able to produce quantitative data throughout its lifetime. This will be achieved with a calibration module that is implemented to perform post-launch calibration, allowing the imager to preserve its ground calibrated 5% radiometric accuracy.

On the optical side there were no specific requirements in the original idea of the instrument besides using as many COTS components as possible to minimise the manufacturing costs of the imager. However, there were other constraints. Firstly, due to having a calibration module that has to be able to move a diffuser and shutter infront of the primary mirror, it limits the maximum size of the mirror to about 4x4 (cm). Secondly, having to fit inside 1U means that it can be difficult to correct for straylight, because the small volume makes it difficult to get rid of the light that is outside of the FOV.

3.2 Requirements

In this section the main requirements are shown. Furthermore, from those requirements new ones were derived and the specific requirements for optics are also written down. The language of requirements is very specific, as it has to be clear what is meant with the requirement. The next list shows the meaning of some specific words:

- SHALL" and "SHALL NOT" are used to indicate a mandatory requirement.
- "SHOULD" and "SHOULD NOT" are used to indicate a recommendation, which is not mandatory.

- ”MAY” and ”NEED NOT” indicate permission or an option.
- ”WILL” indicates a statement of fact or intention. [29]

According to the internal requirement structure, all requirements in this thesis are uniquely numbered and named according to the convention in Table 3.1.

AAA-NNNN	Statement of the requirement	Verification	Backward source
Reasoning of the requirement			

Table 3.1: Requirement structure

Where:

- AAA is the type of requirement according to Table 3.2.
- NNNN is an unique number, where the first number represents the category of the requirement (system, optical, electrical, mechanical, software), the second number represents a subcategory and the final two are progressive numbers within the subcategory.
- Verification defines the verification method according to Table 3.3.
- Backward source is the identifier of the source requirement, if not available N/A is entered.

Abbrevation	Description
FUN	Functional requirement
MIS	Mission requirement
DES	Design requirement
PHY	Physical requirement
INT	Interface requirement
ENV	Environmental requirement
PRA	Product assurance requirement
LGS	Logistical requirement

Table 3.2: Requirement types

Abbrevation	Description
T	Test
A	Analysis
ROD	Review-of-design
I	Inspection
NT	Not trackable

Table 3.3: Types of Verification Methods

Next the primary requirements from the statement of work are listed.

PHY-0000	Size, maximum: 96x96x80 mm g	ROD	N\A
The camera system must fit into allocated space of specified size as a possible main payload of a 2U (min) or 3U (realistic) CubeSat.			

Table 3.4: Volume requirement

PHY-0001	Weight, maximum: 1000 g	ROD	N\A
Weight of the camera system must not exceed the the weight limits imposed on a CubeSat.			

Table 3.5: Mass requirement.

DES-0100	The power consumption of the system should be 1 W at average and 5 W at peak.	ROD	N\A
Power consumption of the camera system must fit into the energy budget of the whole satellite. [RD. 7]			

Table 3.6: Power consumption requirement.

FUN-0200	The EOI shall have an in orbit operational lifetime of at least 3 years.	ROD	N\A
The instrument must survive the launch and in-flight operations for the specified amount of time without excessive degradation which would render it unusable.			

Table 3.7: Lifetime requirement.

FUN-0301	The EOI shall be able to take images over a temperature range of -25°C to 60°C. It supports non-operating temperature range of -40°C to 100°C.	ROD, T	N\A
The camera must support the same temperature ranges, both operating and non-operating, as the satellite. There is a chance that the non-operating temperature is too high. There is usually a good thermal connection between the satellite platform and the payloads, so we are aiming for passive temperature control.			

Table 3.8: Temperature range requirement

FUN-1000	The smeared ground sampling distance shall be at least 100 m at 1000 km and it should be at least 50 m at 600 km.	A	N\A
Minimum for useful remote sensing. This is a requirement that will be optimised for the best performance.			

Table 3.9: GSD requirement

FUN-1001	The FOV shall be a maximum of 10 degrees.	ROD	N\A
This enables the instrument to produce scientific radiometric requirements.			

Table 3.10: FOV requirement

FUN-1002	The EOI shall operate at two spectral bands chosen in cooperation with ESA and to match two Sentinel 2 instrument bands. We propose the bands to be NIR (842-872 nm) and red (645 - 675 nm).	ROD	N\A
Having two spectral bands allows the instrument to be used for NDVI calculation. The bands shall match Sentinel 2 instrument bands to simplify the correlation of the data with current available remote sensing information.			

Table 3.11: Multispectral requirement

FUN-1100	The radiometric resolution should be at least 12 bit.	A	FUN-1101
This enables the instrument to produce scientific radiometric requirements.			

Table 3.12: Radiometric resolution requirement

FUN-1101	The radiometric accuracy shall be at least 5 %	A	N\A
This enables the instrument to produce scientific radiometric requirements.			

Table 3.13: Radiometric accuracy requirement

FUN-1102	The SNR should be minimum 50 at Lref top-of-atmosphere radiance.	A	FUN-1101
This enables the instrument to achieve the stated radiometric accuracy.			

Table 3.14: TOA SNR requirement

From the requirements shown above further more specific requirements were derived from a radiometric budget analysis and keeping the volume and mass constraints in mind.

DES-1200	Optical radiation should be divided into two beams by a dichroic mirror.	ROV	FUN-1002
To maintain light intensity.			

Table 3.15: Dichroic requirement

DES-1201	Standard sizes and COTS parts should be used in optics when possible.	ROD	N\A
To minimise costs.			

Table 3.16: COTS requirement

DES-1202	The mirror substrates should be lightweight, have a relatively high Young's modulus. (Trade-offs shall be considered within the context of the coating and structure material. Possible candidates to be considered should be aluminium and Zerodur.	ROD	PHY-0001
The mirror substrate has to withstand the launch and space environment and also at the same time maintain the required imaging quality.			

Table 3.17: Mirror material requirement

DES-1300	The mirror coating material should have a reflection coefficient of at least 90% at the specified wavelength bands and be resistant to atomic oxygen. Possible candidates for further study should be enhanced aluminium and protected silver.	ROD	FUN-1102
To achieve adequate optical transmission for the desired radiometric resolution and SNR. Furthermore, to not degrade during the expected lifetime of the imager while being subjected to atomic oxygen.			

Table 3.18: Mirror coating reflectivity requirement

DES-1301	The focal length shall be greater than 7.5 cm to achieve the required smeared GSD.	A	FUN-1000
The adequate focal length depends on the dwell time, quantum efficiency, optical transmission and sensor pixel size.			

Table 3.19: Focal length requirement

DES-1302	The aperture ratio should be at least f/4.5 to achieve the required SNR, radiometric resolution, and smeared GSD.	A	FUN-1000, FUN-1102
The adequate aperture ratio depends on the pixel size, optical transmission, spectral band measured, dwell time, quantum efficiency, and sensor noise.			

Table 3.20: Aperture ratio requirement

DES-1400	The sensor pixel size should be at least 6 um to achieve the needed SNR, radiometric resolution and GSD.	A	FUN-1000, FUN-1102
The adequate pixel size for the radiometric resolution and SNR depends on the aperture ratio, optical transmission, spectral band measured, dwell time, quantum efficiency and sensor noise. The adequate pixel size for GSD depends on the focal length and dwell time.			

Table 3.21: Sensor pixel pitch requirement

DES-1401	The quantum efficiency should be at least 20% for NIR and 50% for red to achieve the needed SNR, radiometric resolution and smeared GSD.	A	FUN-1000, FUN-1102
The adequate quantum efficiency depends on the focal length, pixel size, dwell time and spectral band measured. The adequate quantum efficiency for the smeared GSD depends on the focal length, quantum efficiency, optics transmission, dwell time, and pixel size.			

Table 3.22: Sensor QE requirement

DES-1401	The integration time should be be from 0.8 to 2 ms to achieve the needed SNR, radiometric resolution and smeared GSD.	A	FUN-1000, FUN-1102
The adequate dwell time for the SNR and radiometric resolution depends on the focal length, pixel size, quantum efficiency and spectral band measured. The adequate dwell time for the smeared GSD depends on the focal length, quantum efficiency, optics transmission and pixel size.			

Table 3.23: Sensor integration time requirement

4 Design Process

This chapter will elaborate on the design process.

4.1 Design Elements

In this section a trade-off analysis is performed for different optical components, where the selection choice was made by the author of this thesis.

4.1.1 Sensors

There are two sensor types to be considered when imaging in the visible and NIR optical spectrum: charge-coupled device and complimentary metal-oxide-semiconductor sensors. Due to the power consumption requirement DES-0100 (Table 3.6) a low power sensor is preferred. The CMOS sensor was chosen because of its considerably lower power consumption, this is due to the technique of how CCD sensors move the accumulated charge to the analog-to-digital converter. However, CMOS sensors are known to be more noisy. [30] Therefore, it was concluded that a sCMOS sensor should be chosen, given its lower noise levels.

Firstly, a backside illuminated type sensor was chosen to be compliant with DES-1401 (Table 3.22) because the amount of light being reflected into the optical system can be quite low, depending on the spectral band being used and the type of ground coverage being observed. For example, in the current design, one of the bands chosen is 660(30) nm, which is used to observe the light reflected from green vegetation. The amount of reflected light is quite low, about 5% [31]. Thus, the high QE has to be taken as one of the main driving factors in choosing a sensor. This ruled out all the frontside illuminated sensors where the incident photons are frequently blocked by the sensor electronics.

Secondly, to comply with DES-1400 (Table 3.21) pixels have to be bigger than 6 μm, but not too big so that the system becomes non-compliant with FUN-1000 (Table 3.9). Furthermore, with the increase in pixel pitch the sensor size also usually grows, which can make fitting it difficult. However, with bigger pixels the full well capacity of the sensor increases, which increases the saturation level. This meant that a compromise had to be made between having larger pixels, giving us more light per pixel and bigger FWC, but worse GSD, and actually fitting the sensor within the system. An ideal choice would have been about 10 μm pitch and about 800x800 (px), but such a sensor did not seem to exist that would also fit size, QE, and power requirements.

Finally, the chosen sensor was the GSESNSE2020BSI. It is a BSI sCMOS sensor with a 6.5 μm pixel pitch and 2048x2048 (pixels). Even though full sensor illumination cannot be achieved with the current FOV, the sensor itself is small enough that it can easily be fit inside the imager. Compared to regular CMOS sensor this sensor requires more power, but this can be mitigated

with proper duty cycling and other power saving measures. However, this sensor has not been space qualified, but this is not an issue when talking about CubeSats, and the positive properties of the sensor outweighed the fact that it will be tested in flight. [RD. 5]

4.1.2 Mirrors

According to DES-1202 (Table 3.17) the possible substrate materials to be analysed were aluminium and Zerodur. To achieve thermal cohesion with the rest of the aluminium structure of the imager, so that the expansion and contraction due to thermal cycles does not create undue stress on the mirrors and warp their shapes. Thus, aluminium was chosen for the mirror substrate.

Aluminium's reflection coefficient does not satisfy the requirement DES-1300 (Table 3.18) since the reflectance at 660 nm is quite low, about 80% [32]. Given that the design has three mirrors and other optical elements it would give the imager an optical throughput of less than 40%. Transmissivity this low would hinder the radiometric accuracy by degrading the SNR. Thus, a reflectance enhanced coating has to be applied. Research on different coating opportunities was done and it was found that there are choices available that can get the reflectance up to 95%, which would satisfy the requirement [33].

Finally, it is possible to use high order aspherization coefficients or different polynomials for a freeform design to achieve superior optical quality. However, to make the imager cost-effective only conical constants were utilised, since higher order terms change the price of the mirror by an order of magnitude. In future developments of the imager freeform optics can be looked into depending on the manufacturing cost at that time.

4.1.3 Band-pass filters and dichroic mirror

To comply with FUN-1002 (Table 3.11), DES-1200 (Table 3.15), and DES-1201 (Table 3.16). COTS parts were chosen as the spectrum dividing optical elements, which are shown in the bullet list below. However, these can only be used for the prototype imager, because in the straylight analysis it was found that the COTS parts create a substantial ghosting effect in junction with the sensor, which would make the imager non-compliant with requirement FUN-1102 (Table 3.14). This means that all the filters, the dichroic and compensator should have an anti-reflection coating on the side that faces the sensor. The current reflection of the optical elements is about 5%. This should be brought down to about 1-2%. Further analysis is still required for the correct choice of the AR coating. Straylight analysis is out-of-scope for this particular thesis.

The compensator choice is currently a place-holder, since this was added quite late in the design, and further cost related analysis is still to be done. Changing the compensator if needed should not affect the overall design, all of the necessary adjustments can be done either by adjusting the compensator tilt or moving the sensor. Semrock bandpass filters and dichroic were chosen for their high transmission coefficients, the cost-effective possibility of changing the filters physical shape by the manufacturer and having the specific band regions needed for this project. The

two biggest problems with the elements are the transmitted wavefront errors, which affect the optical quality and could be reduced with custom filters, and the dichroic having a very sharp edge in the optical region where it goes from reflective to transmissive. This creates structures in the transmitted and reflected parts of the spectrum, where the coefficients can vary quite significantly, this problem is exaggerated when the angle of incidence is not 45 degrees exactly and can also be affected by the polarization of the incident light. This problem can also be mitigated using custom optical elements with a shallower slope as well as an angle of incidence that corresponds to the optical design.

- Dichroic mirror: Semrock 765 nm BrightLine beamsplitter [34]
- Red band-pass: Semrock 660/30 BrightLine HC [35]
- NIR band-pass: Semrock 857/30 BrightLine HC [36]
- Compensator: Schott SF6G05 radhard glass [37]

4.2 Radiometry

In this section the radiometric budget of the instrument is analysed.

4.2.1 Noise model

According to [26] it is sufficient to consider three noise sources. Firstly, shot noise, which is equal for all sensor types and given by the basic laws of physics, with variance σ_e^2,

$$\sigma_e^2 = K(y - y_{dark}) \tag{4.1}$$

Secondly, all noises coming from sensor readout and amplifier circuits, with variance σ_d^2, and finally the conversion from analog to digital, with variance σ_q^2. This gives us the noise model seen in the equation below:

$$\sigma_y^2 = K\sigma_d^2 + \sigma_q^2 + K(\mu_y - \mu_{y.dark}), \tag{4.2}$$

where

- μ_y - induced electrons in the pixel,
- $\mu_{y.dark}$ - dark current electrons,
- K - gain,
- σ_y^2 - total temporal variance.

4.2.2 Radiometric budget

The main source of noise for any imaging sensor is shot noise, for which the variance is the mean number of incident photons. Thus the longer the integration time, shorter the focal length, bigger the aperture, and better the optical transmission the more electrons we will accumulate which will lead to a proportionally better SNR. The effect of shot noise is large enough that the other sources of noise become marginal. However, some specific considerations still have to be taken in account. Firstly, no two pixels are physically the same, leading to dark signal non-uniformity and photo response non-uniformity. To remove the dark signal, dark frames have to be acquired and can be subtracted from the final images. To remove photo response non-uniformity the relative gains for each pixel have to be found. For that an integrating sphere is used to create a homogeneous light field on the sensor, from which the gains can be calibrated - this is called flat fielding. Both of these remove noise due to non-uniformities but add noise due to the noises not being static, but this impact can be lessened with an increased number of acquired flat-field frames and dark frames. [26]

To calculate the radiometric budget an Excel Worksheet was used that was developed by an ESA engineer Dr. Maurice Borgeaud in 2010 for radiometric budget analysis. This tool takes into account the Sun's spectra, the transmission of Earth's atmosphere, the reflectance of vegetation, orbit height, integration time, and the sensor's QE. With this information the radiometric budget tool calculates the ideal GSD, the smeared GSD due to orbital motion, the SNR of the sensor, and the number of electrons generated. For the SNR calculation the worksheet only uses shot noise, because the other noise sources are comparatively marginal and this is taken to be sufficient to assess the sensor's SNR. The orbit used for the calculation is a 650 km sun-synchronous polar orbit. The optics' transmission factor is taken from the presumption of a 95 % reflectance for the mirrors for both red and NIR spectral bands.

4.2.3 Radiometric budget for the 660(30) nm band

These calculations are based on a reference TOA radiance of $L_{ref} = 20\ Wm^{-2}sr^{-1}\mu m^{-1}$, which means a surface reflectance of about 5%.

Optics transmission factor: $0.95^3(mirrors) * 0.96(dichroicmirror) * 0.95(bandpassfilter) = 0.78$.

In Figure 4.1 below we can see an edited version of the radiometric budget for the 660 nm band using the aforementioned worksheet. The full version can be seen in the appendix. The budget shows that with the current integration time of 4 ms it is possible to achieve an SNR of 70, this is more than the needed 50 TOA SNR, however we need to also take straylight into account, so some margin is needed, and 70 should be sufficient. If it turns out that the SNR has to be increased then there are two ways of doing it. Firstly, the dwell time can still be increased to 4.7 ms, which would be the limit, because going over that the imager would have more than a pixel worth of shift when taking images due to the orbital motion of the spacecraft. Secondly, if it is possible to sample the same ground segment multiple times, then the SNR increases with the square root of the number of frames acquired. Also, we can see that the GSD is 32.4 m and 59.17 m if smearing is also included, thus satisfying the requirement FUN-1000 (Table 3.9) for an orbit height of 1000 km - having a smeared GSD of 75 m, and not satisfying 50 m at an orbit

height of 600 km. This could be corrected by having a smaller integration time or sampling the same surface area multiple times. Furthermore, from the budget it can be seen that at 100 % reflectance (can be even higher for clouds) the sensor would be in saturation, this means that the integration time can be lowered if this turns out to be a problem. Another way to solve this would be to get a sensor with a bigger pixel pitch, resulting in a bigger FWC. However, this would also decrease the GSD due to light being integrated on a bigger area, which could possibly mean that the focal length has to be increased leading to an adjustment in the optical design.

λ start	645		nm
λ end	675		nm
solar power density in this bandwitdh		51,75	Watt/m2
Assumed surface reflectance	0,05		[1]
Focal length	13,05		cm
Lens/aperture diameter	1,88		cm
Pixel pitch	6,5		µm
Satellite height	650		km
Ground sample distance (at nadir)		32,4	m
Atmopshere transmission [%] (assumed)		73,40	[%]
Ground track velocity		6,83	km/s
Solid angle		8,37E-16	rad
Optics transmission factor (BOL=0.783, EOL=0.5)	0,78		[1]
Integration time (<= dwell time)	4,00		ms
Ground resolution (include smearing) at NADIR		59,71	m
Number of available photons		5495	photons
Quantum efficiency of sensor [%] at 660 nm		89,13	%
Number of electrons at reflectance = 0,05		4898	electrons
Number of electrons at reflectance = 1		58774	electrons
SNR of image		70	[1]

Figure 4.1: Edited version of the radiometric budget for 660(30) nm band.

4.2.4 Radiometric budget for the 857(30) nm band

These calculations are based on a reference TOA radiance of $L_{ref} = 100\ Wm^{-2}sr^{-1}\mu m^{-1}$, corresponding to a surface reflectance of 36%.

Optics transmission factor: $0.95^3(mirrors) * 0.97(dichroicmirror) * 0.97(bandpassfilter) * 0.96(compensator) = 0.79$.

In Figure 4.2 an edited version of the radiometric budget for the 857 nm band can be seen. The full version can be seen in the appendix. The budget shows that with the same parameters as for the red band, it is possible to achieve an SNR of 137. Since wavelength does not affect the GSD it is the same as for the 660(30) nm band. However, as is evident from the budget at 100 % reflectance, the NIR band sensor does not reach saturation level, because of the sensor's lower

QE in that part of the spectrum, even though more energy is reflected by vegetation in the NIR.

λ start	842		nm
λ end	872		nm
solar power density in this bandwitdh		35,85	Watt/m2
Assumed surface reflectance	0,36		[1]
Focal length	13,05		cm
Lens/aperture diameter	1,88		cm
Pixel pitch	6,5		µm
Satellite height	650		km
Ground sample distance (at nadir)		32,4	m
Atmopshere transmission [%] (assumed)		72,33	[%]
Ground track velocity		6,83	km/s
Solid angle		8,37E-16	rad
Optics transmission factor (BOL=0.783, EOL=0.5)	0,78		[1]
Integration time (<= dwell time)	4,00		ms
Ground resolution (include smearing) at NADIR		59,71	m
Number of available photons		35071	photons
Quantum efficiency of sensor [%] at 857 nm		53,23	%
Number of electrons at reflectance = 0,36		18666	electrons
Number of electrons at reflectance = 1		31111	electrons
SNR of image		137	[1]

Figure 4.2: Edited version of the radiometric budget for 857(30) nm band.

4.3 Optical Design

The chosen design for the system is an unobscured three mirror anastigmat. A reflective system was used to minimise the effects of chromatic aberration when using different spectral bands, which makes it possible to swap out the bandpass filters without having to significantly change alignment. The design with three mirrors was chosen because it minimises the main aberrations, while having a few degrees of freedom still left to configure the system to fit the needs of the design [38]. Also, using more than three mirrors reduces the optical transmission of the system, which can become detrimental to the SNR of some spectral bands. The unobscured version of the design was chosen since the aperture is quite small due to the form factor and fitting in the calibration unit, which means that diffraction would have a significant impact on the optical quality. The parameters of the design can be seen in the table below. The rounding was done corresponding to presumed manufacturing capabilities.

EFL	-130.5 mm
F#	4.91
Full FOV	2.1 deg x 2.7 deg (rectangular)
Primary mirror radius	-180.778 mm
Secondary mirror radius	-73.184 mm
Tertiary mirror radius	-117.619 mm
Primary mirror conic constant	-1.639081 (hyperbola)
Secondary mirror conic constant	-1.4653326 (hyperbola)
Tertiary mirror conic constant	-0.3712524 (ellipse)

Table 4.1: Optical design parameters

As seen from Table 4.1 the system is compliant with the requirements FUN-1001 (Table 3.10), and DES-1301 (Table 3.9), but non-compliant with the requirement DES-1302 (Table 3.20). The deviation from the required F# is insignificant, and the resulting decrease in available energy was rectified with a longer exposure time.

The main considerations for the design were compactness, optical quality, and a long back focal length to fit the filters, the dichroic mirror, and the compensator for it. A compact design can be achieved with a concave - convex - concave mirror choice. [39] The optical quality was optimised for a long back focal length, and to achieve that, the Rosetta narrow angle camera was taken as the baseline design [40], which had also been optimised for a long BFL. This design was put into OSLO optical design software and optimised for the specific needs of this project. The optimisation was done by constructing an error function based on the WFE, the deviation from a 130 mm focal length, and the angle of incidence for the bandpass filters and the dichroic. Different optimisation algorithms were used inside the program, to end up with a system that is in a local minimum and most likely also close to the global minimum. In Figure 4.3 the YZ-plane view of the NIR band optical path is seen and in Figure 4.4 the XZ-plane view of the red band optical path can be seen. The mirrors are depicted in scale, but other component sizes are exaggerated. The aperture can be seen as the line in front of the main mirror as the idea was to have the main mirror as the aperture stop.

To get a better understanding of the system Figure 4.5 shows the imager in operational mode and Figure 4.6 shows the inner workings of the imager.

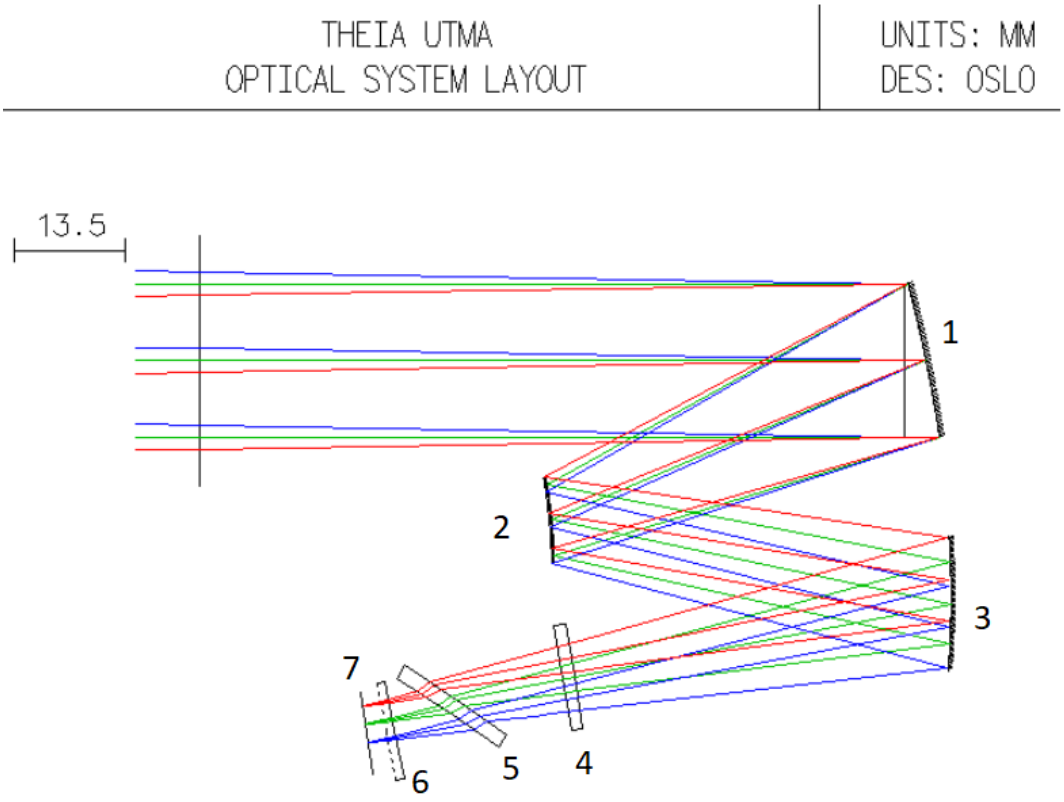

Figure 4.3: YZ-layout of the optical design, where 1 - primary mirror, 2 - secondary mirror, 3 - tertiary mirror, 4 - dichroic mirror, 5 - compensator for the dichroic, 6 - 857 nm bandpass filter, 7 - image plane.

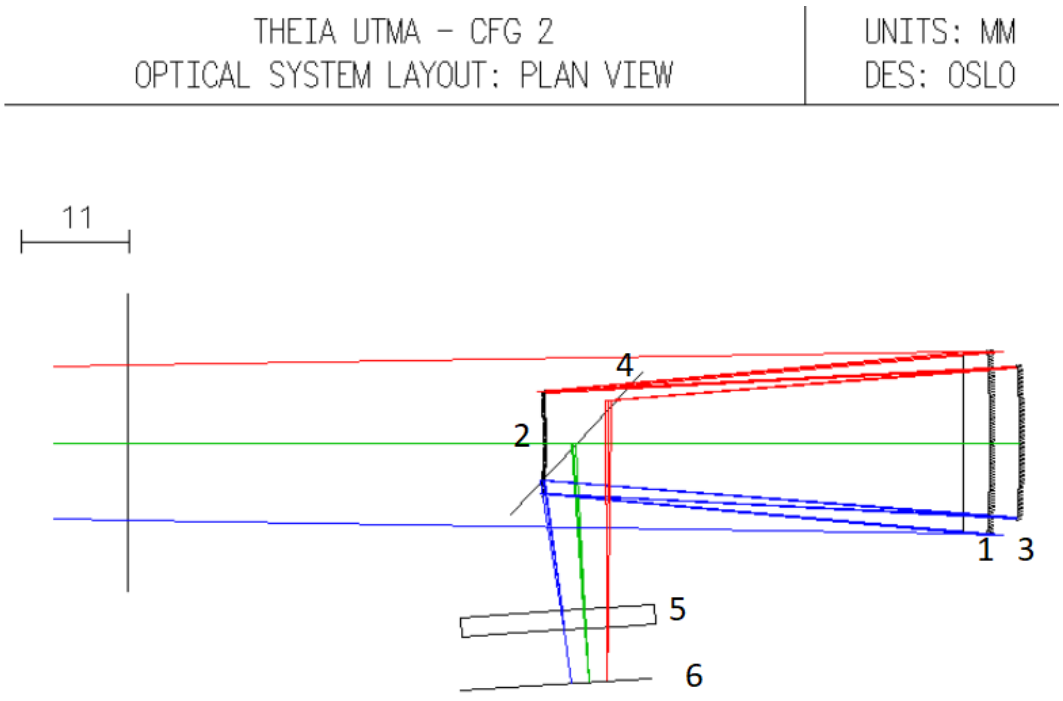

Figure 4.4: XY-layout of the optical design, where 1 - primary mirror, 2 - secondary mirror, 3 - tertiary mirror, 4 - dichroic mirror, 5 - 660 nm bandpass filter, 6 - image plane.

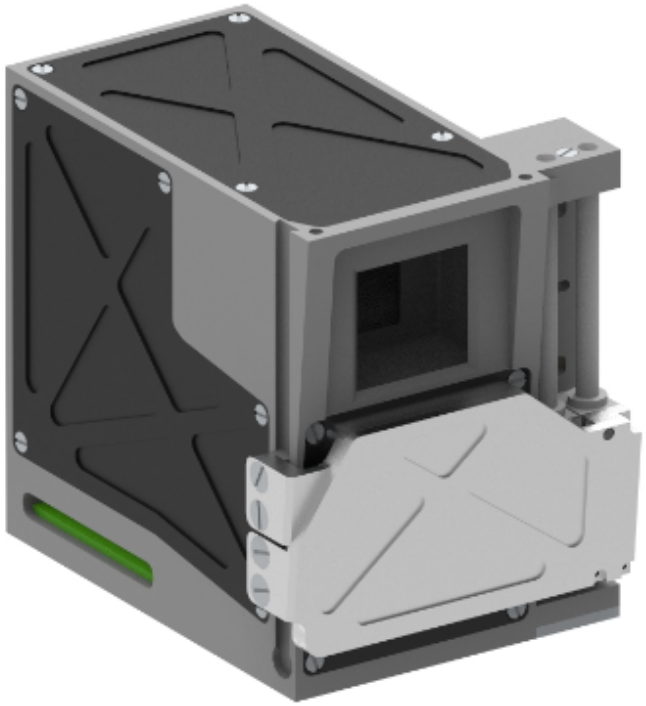

Figure 4.5: Imager in operational mode

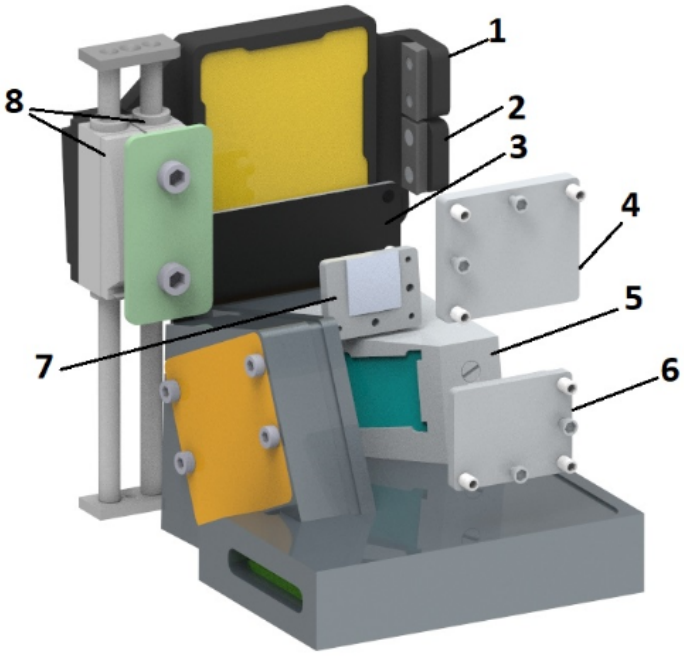

Figure 4.6: The interior of the EOI - diffuser(1), shutter(2), front cover(3), primary mirror(4), beamsplitter assembly(5), tertiary mirror(6), secondary mirror(7), actuators(8) to move the calibration module

4.4 Optical Performance Analysis

The main consideration in optical quality and tolerancing is the Marechal criterion which states that the Strehl ratio should be at least 0.8. We will look at this condition from the perspective of RMS wavefront error, which has to be less than 0.07 λ to meet the criterion. For most of the analysis 9 field points are used , one corresponding to the centre of the sensor, 4 corresponding to the edges of the FOV, and 4 corresponding to the diagonal corners of the FOV. These were chosen to get good estimation of the performance on the whole focal plane. However, for telecentricity, MTF and RMS WFE more field points were chosen.

4.4.1 Spot diagram relative to field of view

Spot diagram is a collection of ray data resulting from tracing a large number of rays from a single object point through the aperture of the system. The resulting plots shown in Figure 4.7 and Figure 4.8 show the geometric ray distribution, but do not necessarily indicate the irradiance distribution, because there is no weighing of the rays. [20] The Airy disk in the plots is represented by the black circles. The figures show that the current design is diffraction limited.

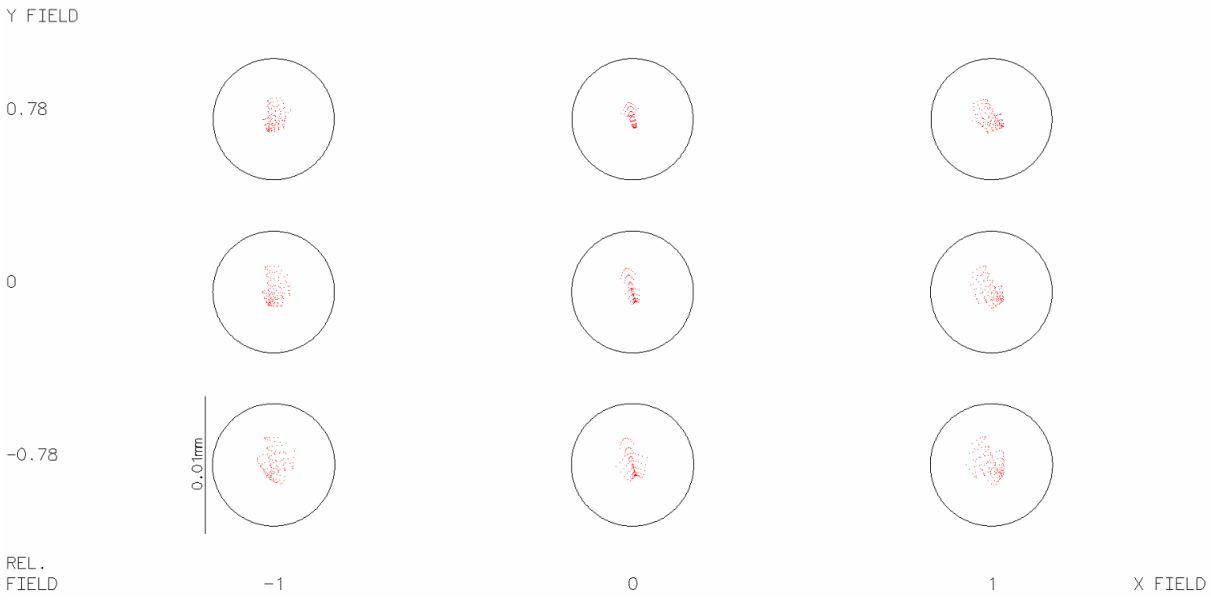

Figure 4.7: Spot diagrams for the red band vs the relative FOV of 1.35 degrees.

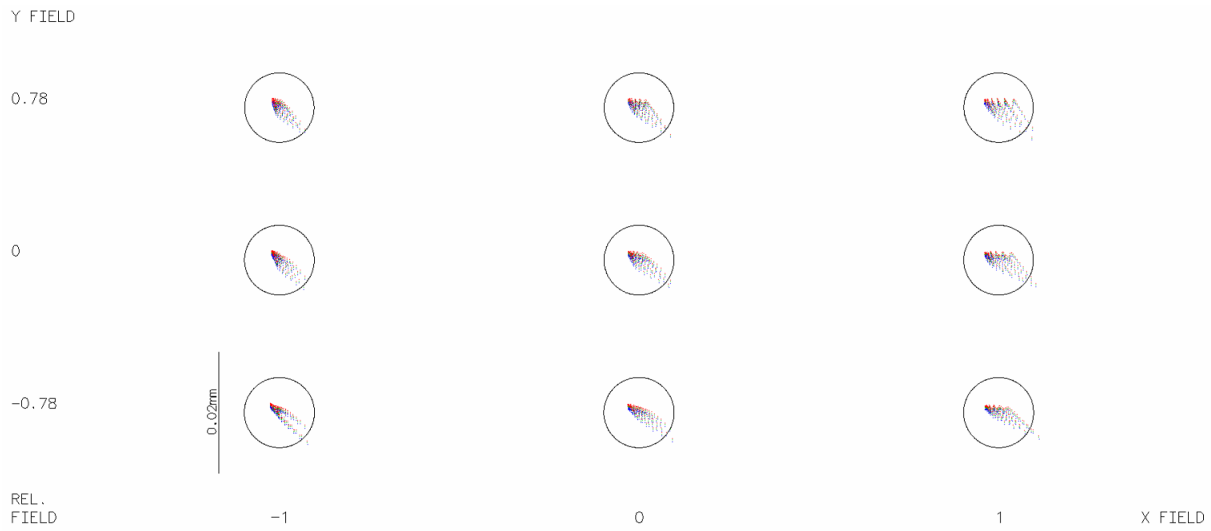

Figure 4.8: Spot diagrams for the NIR band vs the relative FOV of 1.35 degrees.

4.4.2 Point spread function relative to FOV

A more adequate evaluation of image quality than the spot diagra is the PSF calculation. PSF diagrams are shown by Figure 4.9 and Figure 4.10 for the 660(30) nm and 857(30) nm band respectively. The size of the squares in the plot is 2x2 (pixels), as this is the ideal case defined by the Nyquist criterion to adequately sample a signal. What to look for in PSF plots is the focused shape of the distributions so that they have one maxima that is in the center of the spread. As it is evident from the figures - the PSFs do not fill the 2x2 (pixel) grid as would be most effective, which means the system will be undersampled, but this should not affect the performance of the system. Also, all the PSFs have a well-defined structure with the energy concentrated in the center.

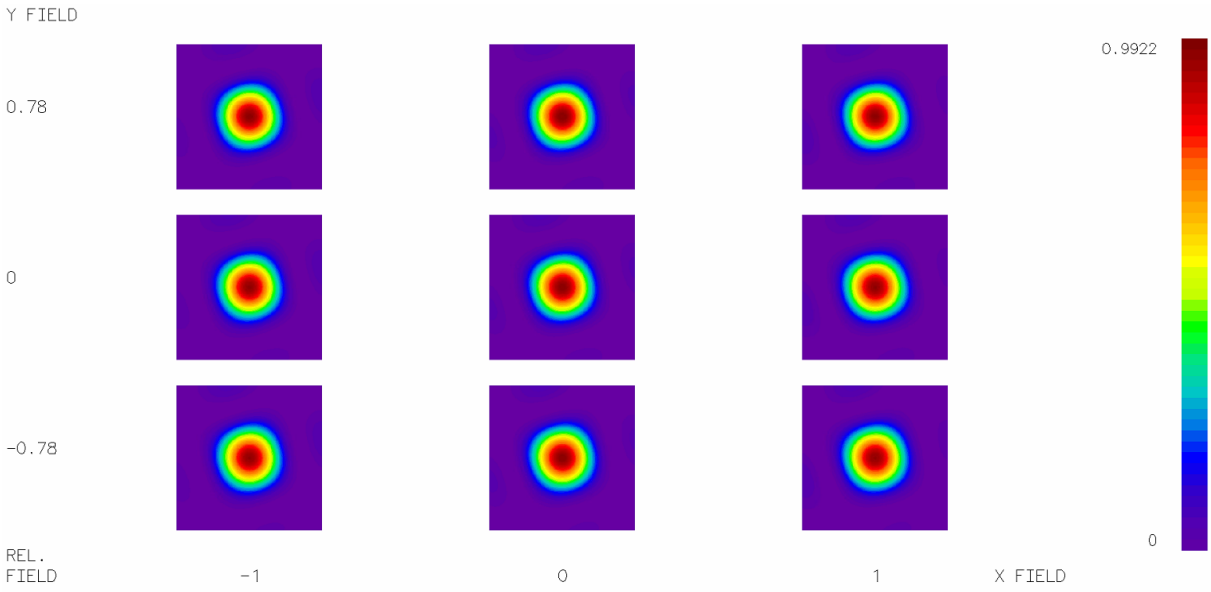

Figure 4.9: PSF for the red band vs the relative FOV of 1.35 degrees.

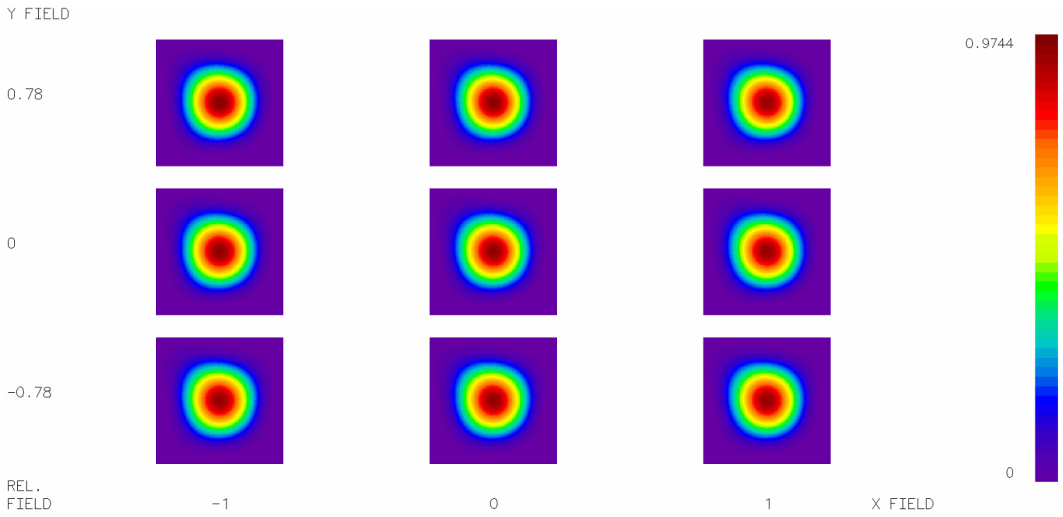

Figure 4.10: PSF for the NIR band vs the relative FOV of 1.35 degrees.

4.4.3 Modulation transfer function relative to the FOV

There are no specific requirements for the MTF, but the goal is to achieve a similar total system MTF as the Sentinel-2 Multispectral Instrument for the respective bands. If the imager achieves the same MTF at the sensor's Nyquist frequency, then it can be concluded to be sufficient for the imager. For Sentinel-2 it is between 0.15...0.3 [41]. In Figure 4.11 and Figure 4.12 the MTF of the system is plotted relative to its FOV at the Nyquist frequency. It can be seen that the MTF is about 0.6 for the 660 nm band and 0.5 for the 857 nm band. This means that the MTF of the sensor should be at least 0.3 for the 857 nm band and 0.25 for the 660 nm band. The GSENSE2020BSI sensor MTF values are 0.33 and 0.28 respectively so, the sensor can be used in the design. Based on this, we can say that the design achieves the optimal range for the MTF.

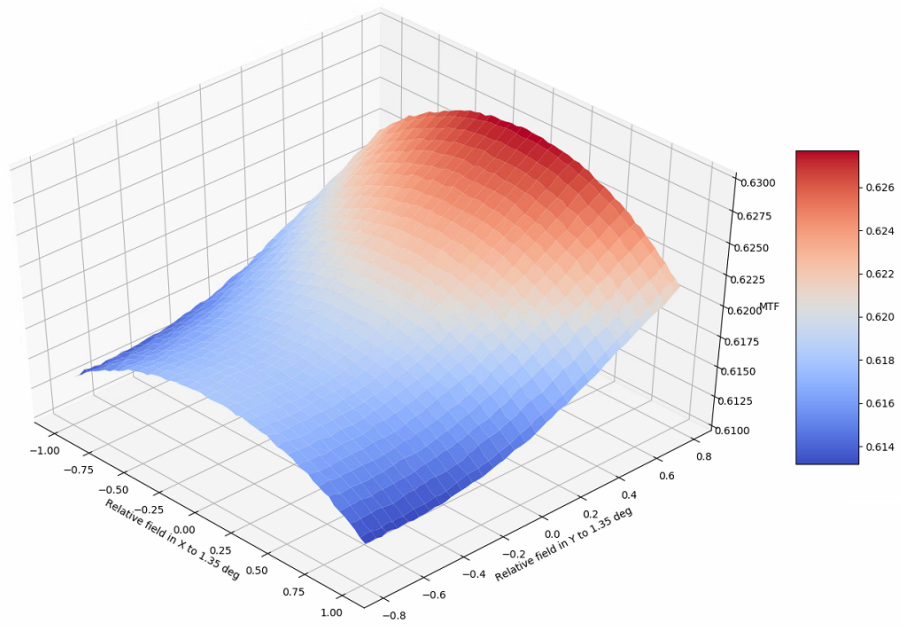

Figure 4.11: MTF at 77 Hz for the red band vs the relative FOV of 1.35 degrees.

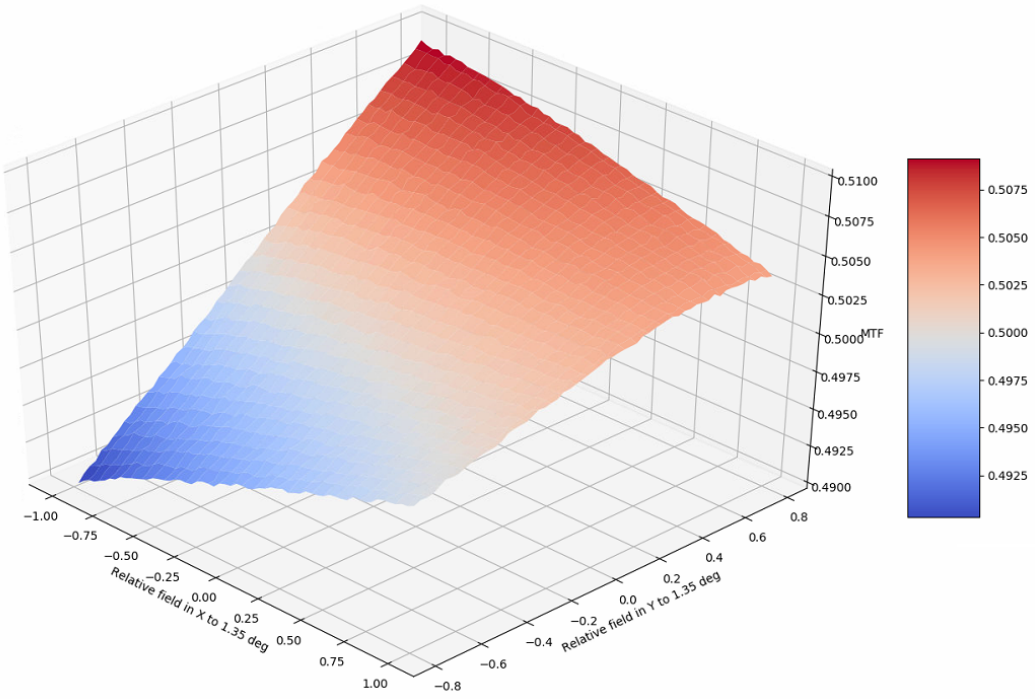

Figure 4.12: MTF at 77 Hz for the NIR band vs the relative FOV of 1.35 degrees.

4.4.4 Distortion

Distortion is a geometrical aberration that shows the deviation from a rectilinear projection. [20] It is preferred that the projection is orthogonal to the sensor. The distortion we see in Figure 4.13 and Figure 4.14 is small enough that it can be corrected with software, by characterising the manufacutred imager's distortion and finding the corrective function or functions to apply to the captured frames.

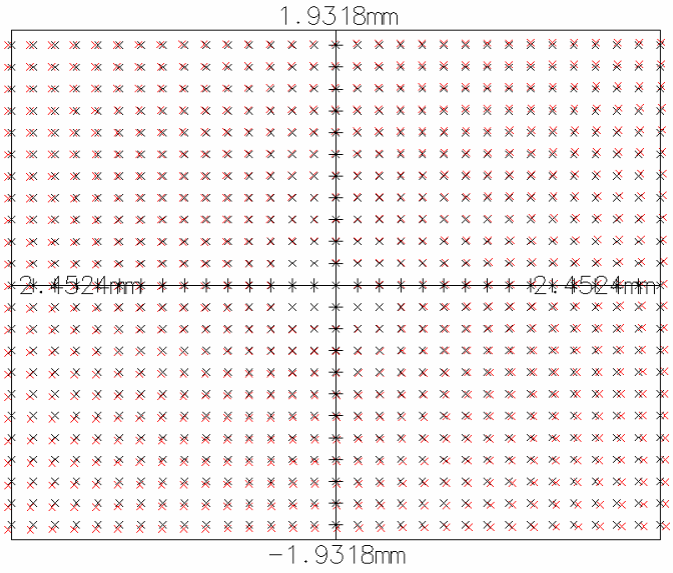

Figure 4.13: Distortion for the red band vs the relative FOV of 1.35 degrees.

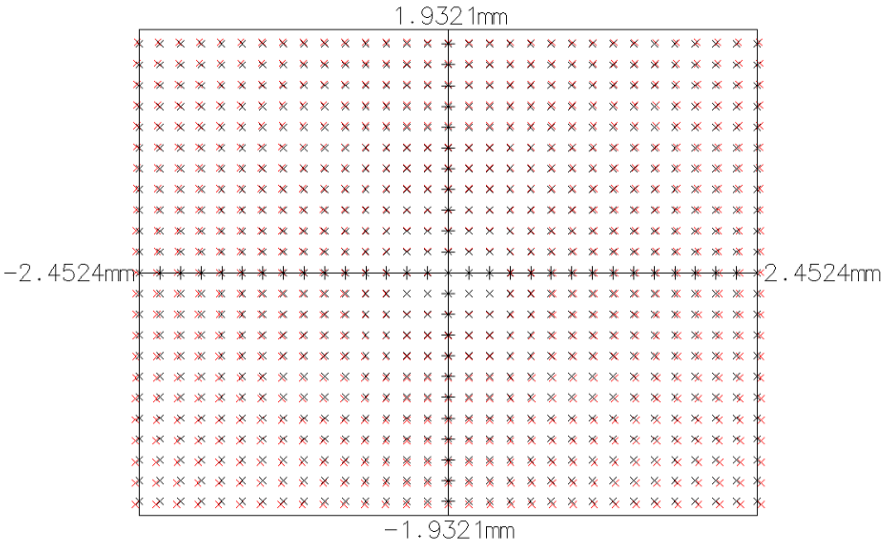

Figure 4.14: Distortion for the NIR band vs the relative FOV of 1.35 degrees.

4.4.5 RMS Wavefront Error relative to the FOV

RMS WFE is the deviation of the wavefront from a perfect sphere caused by the optical system. [20] As mentioned before, the RMS WFE should be kept below 0.07 λ for a diffraction limited system. As can be seen from Figure 4.15 and Figure 4.16 the imager in its ideal state satisfies this criterion throughout the FOV.

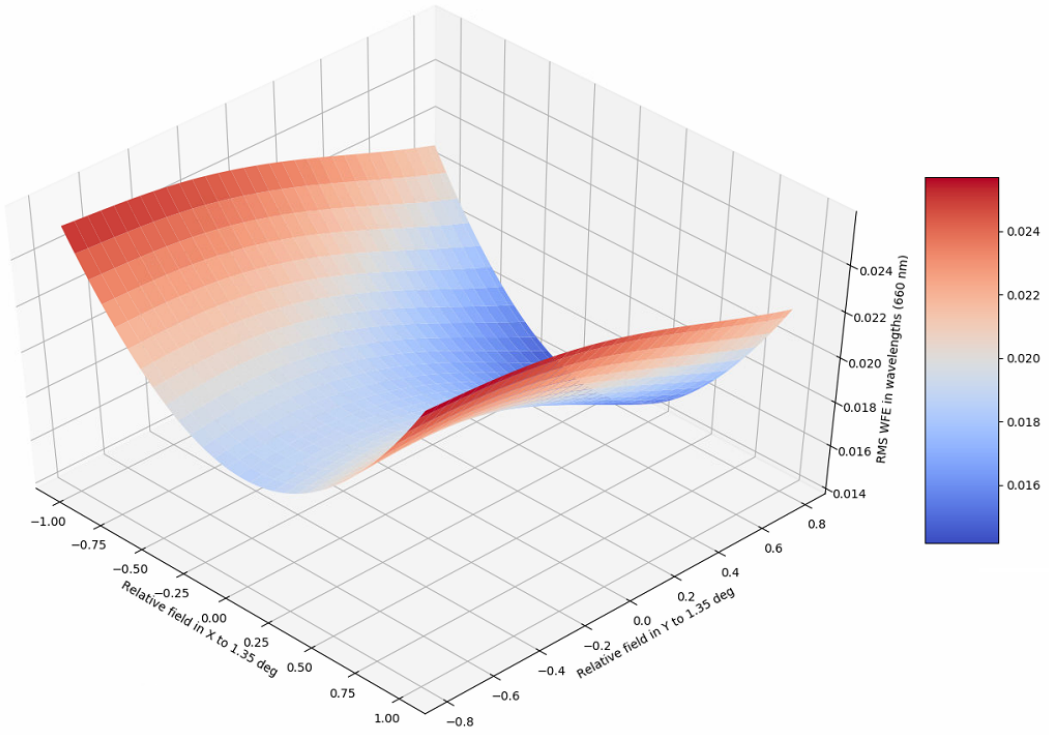

Figure 4.15: RMS WFE for the red band vs the relative FOV of 1.35 degrees.

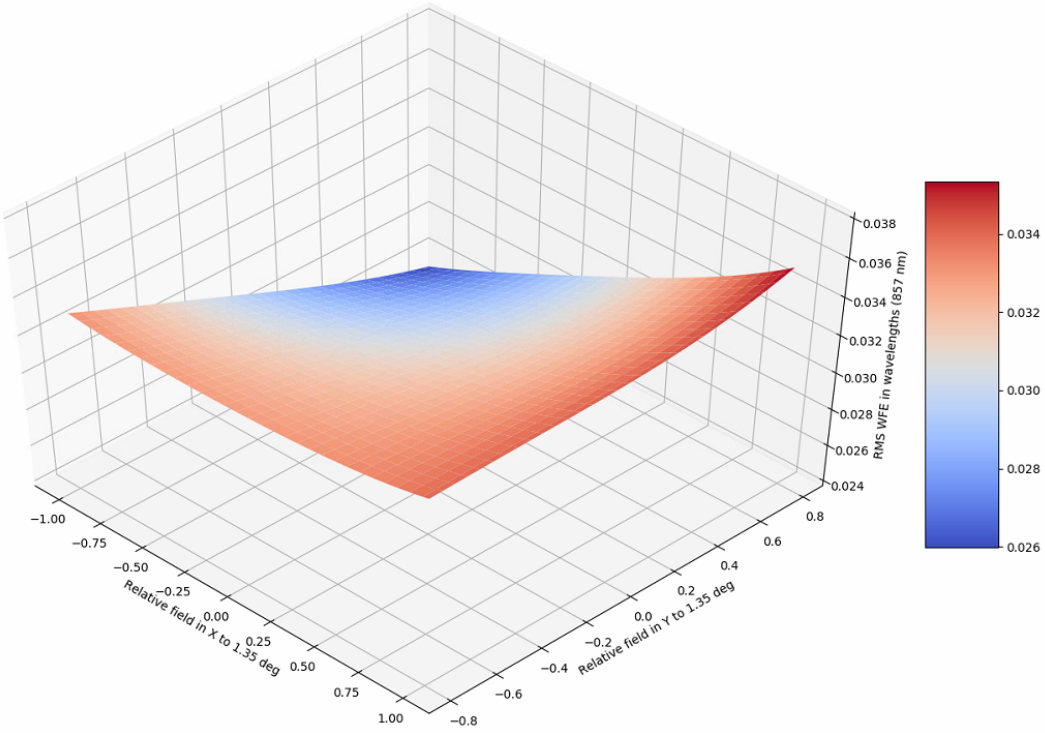

Figure 4.16: RMS WFE for the NIR band vs the relative FOV of 1.35 degrees.

4.4.6 Telecentricity

To characterise the telecentricity of the system the chief ray angle is chosen. This is important for different reasons. Firstly, the QE of the sensor is angle dependent. So, if the angles of the light bundles incident on the sensor vary significantly it will affect the accuracy of the measurements. Secondly, the spectral bands that the bandpass filters transmit depend on a few factors, one of them being the angle of incidence [42]. Here again, if the AOI varies for different ray bundles then different parts of the sensor will receive different spectral information. This is called out-of-band contribution and it cannot be corrected meaning the imager would have an added source of noise. From Figure 4.17 and Figure 4.18 below it can be seen that from one edge of the FOV to the other the chief ray angle changes about 1 degree, which was decided to be sufficiently telecentric.

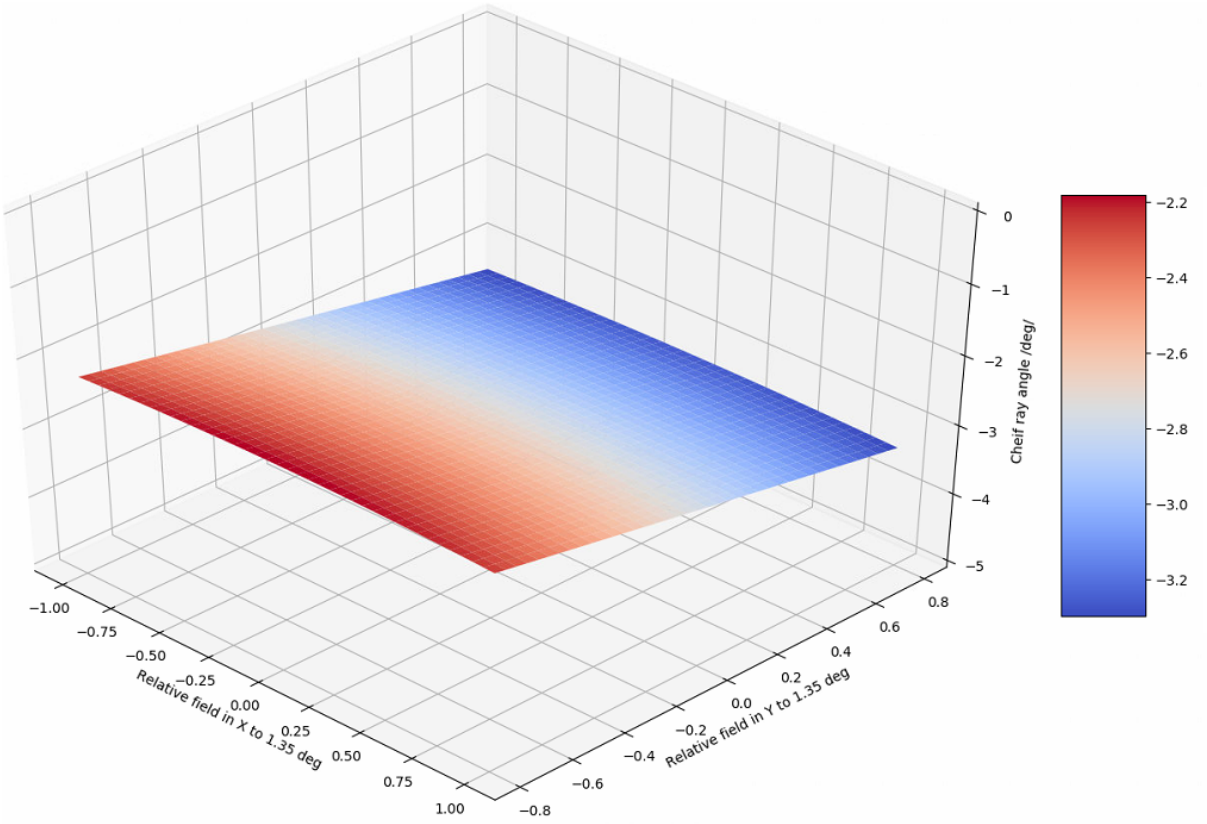

Figure 4.17: Chief ray angle for the red band vs the relative FOV of 1.35 degrees.

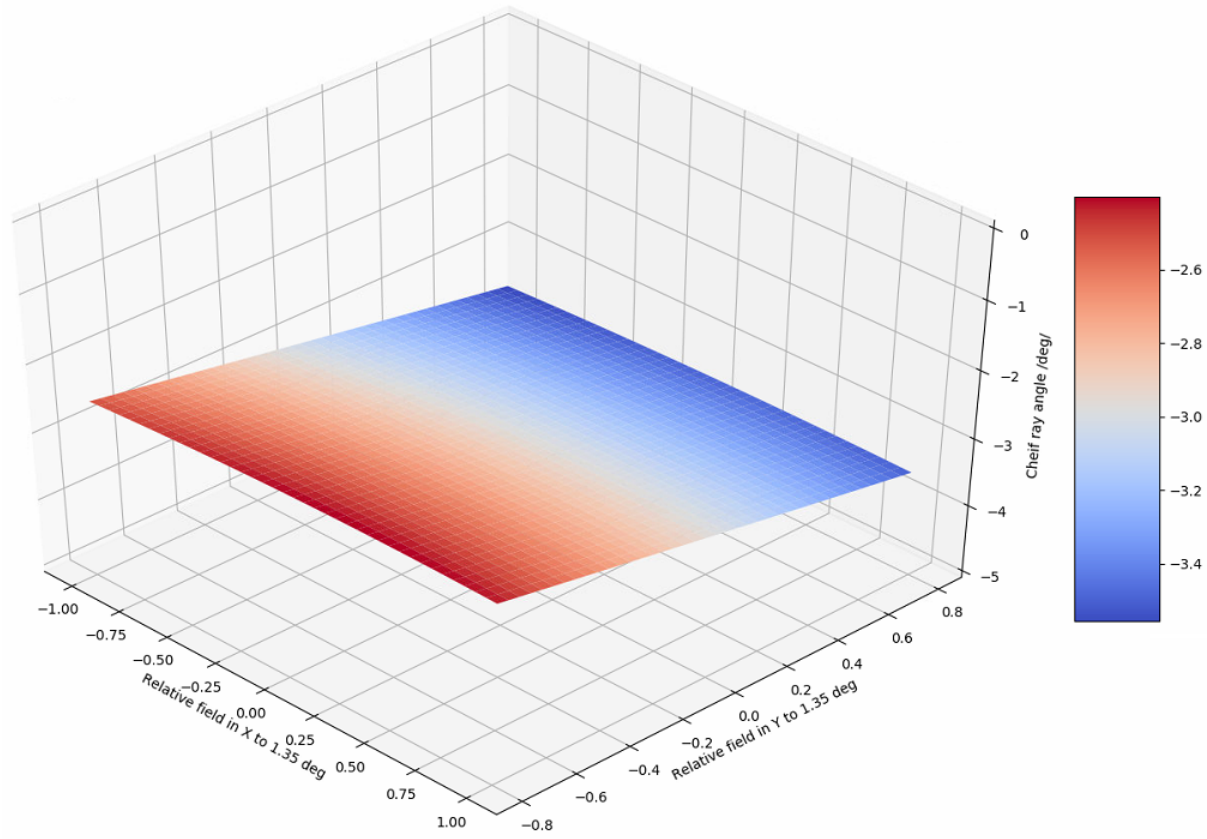

Figure 4.18: Chief ray angle for the NIR band vs the relative FOV of 1.35 degrees.

4.5 Tolerancing Analysis

In this chapter analysis has been performed to see how the system's optical quality changes with respect to presumed manufacturing tolerances.

4.5.1 Surface Form Error Map Tolerancing

To simulate the error in the surface shape due to manufacturing uncertainty, random surface form error maps were generated using asymmetric Zernike polynomials (Z4-Z36). The coefficients were normalised to 100 nm RMS (their sum is 100e-9), as this was seen as the possible manufacturing tolerance. All of the tolerance analysis shown below have the surface form error applied to the mirrors. Therefore, plots specifically for the WFE resulting from the SFE are not shown.

4.5.2 Manufacturing Tolerances

The presumed manufacturing and alignment tolerances used in the tolerancing sensitivity analysis are listed in Table 4.2. Two main degrees of freedom were not taken into account for tolerances, namely the change in radius of curvature and the change in conic constant. Firstly, changing the curvature also changes the focal distance, thus resulting in a big defocus error term, which can be corrected with correctly aligning the sensor. Since it is not possible to compensate for the defocus during the tolerancing analysis, with the software used, this was left out. Secondly, the conic constant error is simulated using the SFE maps, so there is no need to have a second tolerance for it.

As seen from the results in Table 4.3 and Table 4.4, deviations from the theoretical optical design for each DOF by the tolerance amount the system is still within the Marechal criterion. However, in this analysis only one DOF is perturbed at a time, and because different deviations from the original design do not add up linearly, a Monte Carlo analysis has to be performed on the imager as well.

Degree of freedom	**Tolerance**
Translations	10 μm
Rotations	0.01 degrees
Thicknesses	10 μm

Table 4.2: Presumed manufacturing and alignment tolerances

Relative field in Y to 1.35 deg	Relative field in X to 1.35 deg	Nominal RMS (λ)	High RMS w/ Tols (λ)	Mean Change (λ)	Std Dev (λ)
0	0	0.018	0.059	0.015	0.006
0	1	0.029	0.059	0.010	0.010
0	-1	0.028	0.058	0.011	0.009
0.78	0	0.013	0.042	0.017	0.006
0.78	1	0.027	0.054	0.011	0.008
0.78	-1	0.026	0.053	0.011	0.008
-0.78	0	0.018	0.047	0.015	0.006
-0.78	1	0.031	0.062	0.011	0.010
-0.78	-1	0.031	0.061	0.011	0.010

Table 4.3: Tolerancing sensitivty analysis for the red band using presumed manufacturing and alignment tolerances, showing the worst case WFE.

Relative field in Y to 1.35 deg	Relative field in X to 1.35 deg	Nominal RMS (λ)	High RMS w/ Tols (λ)	Mean Change (λ)	Std Dev (λ)
0	0	0.031	0.049	0.009	0.004
0	1	0.036	0.054	0.006	0.005
0	-1	0.029	0.043	0.007	0.003
0.78	0	0.031	0.045	0.07	0.003
0.78	1	0.039	0.057	0.006	0.006
0.78	-1	0.024	0.039	0.008	0.003
-0.78	0	0.034	0.048	0.007	0.004
-0.78	1	0.035	0.050	0.007	0.004
-0.78	-1	0.035	0.052	0.007	0.005

Table 4.4: Tolerancing sensitivty analysis for the NIR band using presumed manufacturing and alignment tolerances, showing the worst case WFE.

4.5.3 Monte Carlo Analysis

A Monte Carlo analysis was performed using 1000 randomly perturbed optical systems. The error function depicted in Figure 4.20 and is the RMS WFE of the respective band. The nominal RMS WFEs are 0.031 λ for the 857(30) nm band and 0.026 λ for the 660(30) nm band. As seen from the figures the RMS WFE most likely will stay near the nominal value, and even in edge cases it will still most likely stay inside the diffraction limit. Thus, we can conlude that even with taking into account the various disturbances according to the tolerances given, the EOI's optical quality achieves the initial requirements.

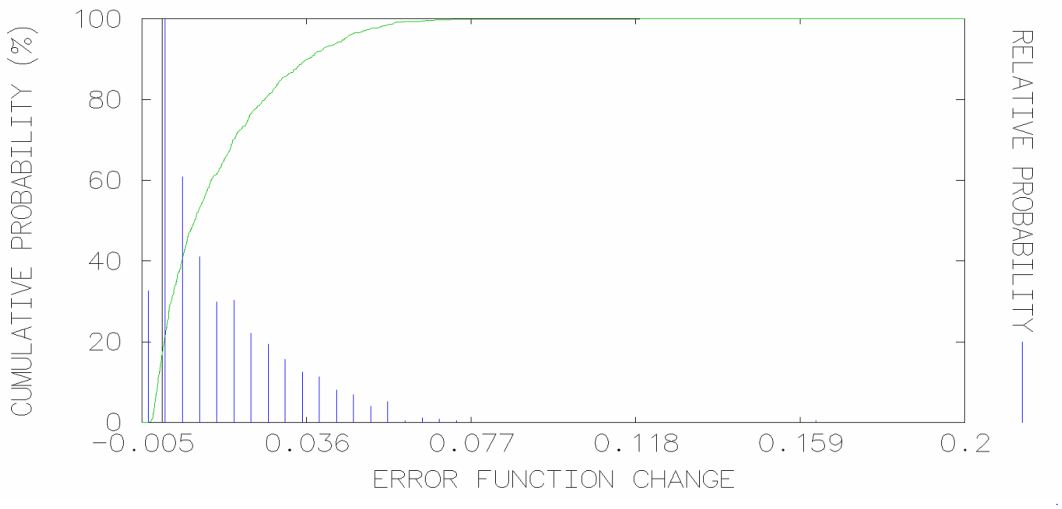

Figure 4.19: Monte Carlo analysis using 1000 systems with the presumed manufacturing and alignment tolerances for the red band. The nominal RMS WFE was 0.026 λ.

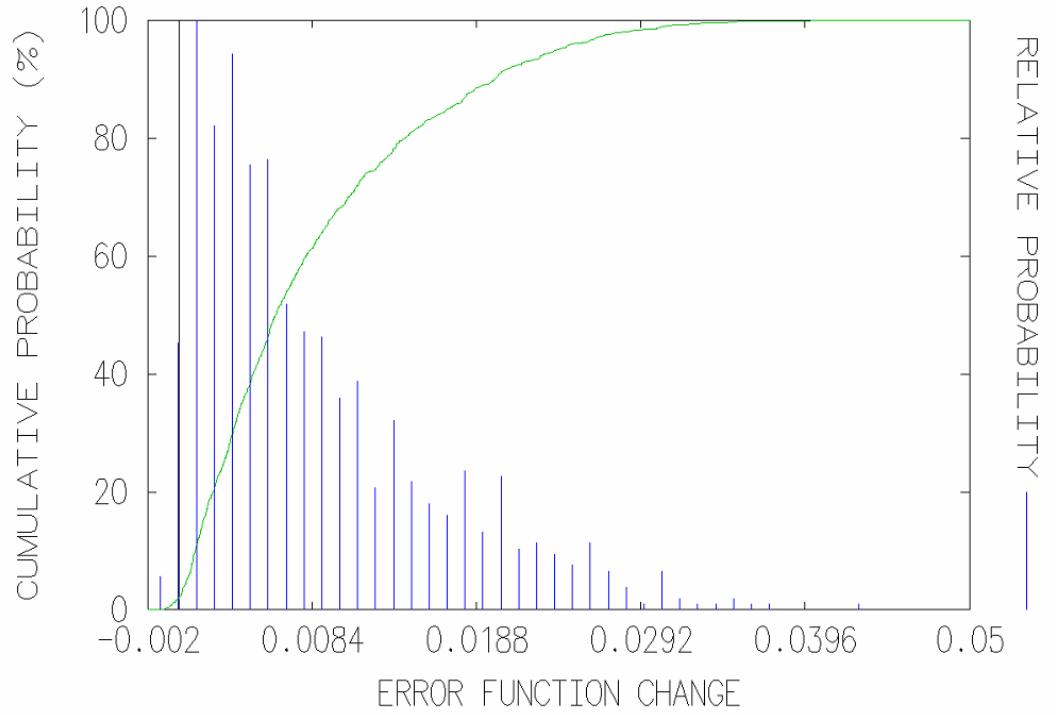

Figure 4.20: Monte Carlo analysis using 1000 systems with the presumed manufacturing and alignment tolerances for the NIR band. The nominal RMS WFE was 0.031 λ

5 Conclusions and Future Work

In this thesis a diffraction limited optical design for a 1U sized radiometrically calibrated multispectral Earth observation imager for nanosatellites is demonstrated and its performance analysed. The design was achieved by gathering a list of optical and radiometric requirements based off the original proposal and further elaborating on them based on a radiometric budget analysis. In the budget an assumption of sensing vegetation to calculate the NDVI was made. Moreover, in parallel with the radiometric budget analysis, other optical components that are part of the imaging pipeline were chosen, such as the sCMOS sensor. Furthermore, a tolerancing analysis was performed using presumed manufacturing and assembly tolerances. The analysis showed that the contributions to the wavefront error were sufficiently small, such that the imager can be manufactured while maintaining the optical quality. However, the optical design is non-compliant with two of the optical requirements, these are seen as minor non-compliances and do not affect the goal of the project.

The project will continue by the Autumn of 2019 at the latest, at which point manufacturing will begin followed by assembly, testing, characterisation, and calibration. The plans for calibration and testing have already been made and most of the procedures will be verified on the ESTCube-2 Earth observation payload. The tests for it will begin in the Summer of 2019.

Acknowledgements

I would like to thank my supervisors Hendrik Ehrpais, who has been a great team lead and supervisor since I started at ESTCube three years ago and Nikolay Voznesenskiy, who has helped me better understand the concepts in optics. Furthermore, I am greatful for the people in the project team: Silvar Muru, Madis Kaspar Nigol, Hans Sams and Reimo Soosaar. Lastly, I would like to thank ESA for accepting this project and our contact personnel Berit Ahlers and Micael Miranda for helping us realise it.

Bibliography

[1] S. Lee, A. Hutputanasin, A. Toorain, W. Lan, R. Munakata, J. Carnahan, D. Pignatelli, A. Mehrparvar, Cubesat design specification rev 13, Tech. rep., California Polytechnic State University (2014).

[2] E. Kulu, Nanosats database (visited 16.05.2019).
URL https://www.nanosats.eu/

[3] J. Nielsen, J. Larsen, J. Grunnet, M. Kragelund, A. Michelsen, K. Kjaer Sørensen, Aausat-ii, a danish student satellite, I S A S Nyusu.

[4] H. J. Kramer, ALL-STAR(Agile Low-cost Laboratory for Space Technology Acceleration and Research) (visited 20.05.2019).
URL https://earth.esa.int/web/eoportal/satellite-missions/a/all-star

[5] A. Slavinskis, M. Pajusalu, H. Kuuste, E. Ilbis, T. Eenmäe, I. Sünter, K. Laizans, H. Ehrpais, P. Liias, E. Kulu, J. Viru, J. Kalde, U. Kvell, J. Kütt, K. Zalite, K. Kahn, S. Lätt, J. Envall, P. Toivanen, J. Polkko, P. Janhunen, R. Rosta, T. Kalvas, R. Vendt, V. Allik, M. Noorma, Estcube-1 in-orbit experience and lessons learned, IEEE Aerospace and Electronic Systems Magazine 30 (8) (2015) 12–22. doi:10.1109/MAES.2015.150034.

[6] H. J. Kramer, Planet - Flock Imaging Constellation (visited 20.05.2019).
URL hhttps://directory.eoportal.org/web/eoportal/satellite-missions/f/flock-1

[7] M. Soukup, J. Gailis, D. Fantin, A. Jochemsen, C. Aas, P.-J. Baeck, I. Benhadj, S. Livens, B. Delauré, M. Menenti, B. Gorte, S. Hosseini aria, M. Esposito, C. van Dijk, Hyperscout: Onboard processing of hyperspectral imaging data on a nanosatellite, 2016.

[8] M. C. Hansen, T. R. Loveland, A review of large area monitoring of land cover change using landsat data, Remote Sensing of Environment 122 (2012) 66 – 74, landsat Legacy Special Issue. doi:https://doi.org/10.1016/j.rse.2011.08.024.

[9] M. Claverie, V. Demarez, B. Duchemin, O. Hagolle, D. Ducrot, C. Marais-Sicre, J.-F. Dejoux, M. Huc, P. Keravec, P. Béziat, R. Fieuzal, E. Ceschia, G. Dedieu, Maize and sunflower biomass estimation in southwest france using high spatial and temporal resolution remote sensing data, Remote Sensing of Environment 124 (2012) 844 – 857. doi:https://doi.org/10.1016/j.rse.2012.04.005.

[10] E. K. Melaas, M. A. Friedl, Z. Zhu, Detecting interannual variation in deciduous broadleaf forest phenology using landsat tm/etm+ data, Remote Sensing of Environment 132 (2013) 176 – 185. doi:https://doi.org/10.1016/j.rse.2013.01.011.

[11] M. Wall, NASA Launches Advanced Landsat Earth-Watching Satellite into Orbit (visited 20.05.2019).
URL https://www.scientificamerican.com/article/nasa-launches-advanced-landsat/

[12] S. Clark, 'Europe's Landsat' in the starting blocks (visited 20.05.2019).
URL https://spaceflightnow.com/2015/06/21/europes-landsat-in-the-starting-blocks/

[13] M. Hank Heidt, P. Puig-suari, P. Augustus, S. Moore, P. Shinichi Nakasuka, P. Robert, J. Twiggs, Cubesat: A new generation of picosatellite for education and industry low-cost space experimentation.

[14] M. Drusch, U. D. Bello, S. Carlier, O. Colin, V. Fernandez, F. Gascon, B. Hoersch, C. Isola, P. Laberinti, P. Martimort, A. Meygret, F. Spoto, O. Sy, F. Marchese, P. Bargellini, Sentinel-2: Esa's optical high-resolution mission for gmes operational services, Remote Sensing of Environment 120 (2012) 25 – 36, the Sentinel Missions - New Opportunities for Science. doi:https://doi.org/10.1016/j.rse.2011.11.026.

[15] W. J. Smith, Modern Optical Engineering - The Design of Optical Systems, 3rd Edition, McGraw-Hill, New York, 2000.

[16] E. W. Weisstein, Chied ray (visited 17.05.2019).
URL http://scienceworld.wolfram.com/physics/ChiefRay.html

[17] Edmund optics, The advantages of telecentricity (visited 17.05.2019).
URL https://www.edmundoptics.com/resources/application-notes/imaging/advantages-of-telecentricity/

[18] Edmund optics, Limitations on resolution and contrast: The airy disk (visited 17.05.2019).
URL https://www.edmundoptics.com/resources/application-notes/imaging/limitations-on-resolution-and-contrast-the-

[19] E. L. Dereniak, T. D. Dereniak, Geometrical and Trigonometric Optics, Cambridge University Press, 2008. doi:10.1017/CBO9780511755637.

[20] Lambda Research Corporation, OSLO Optics Reference.

[21] Geometrical product specification, Tech. rep., ISO/TC 213 Dimensional and geometrical specifications and verification (Dec. 2011).

[22] R. Rottenfusser, E. E. Wilson, M. W. Davidson, The point spread function (visited 17.05.2019).
URL https://www.zeiss.com/microscopy/us/solutions/reference/basic-microscopy/the-point-spread-function.html

[23] Edmund optics, Introduction to modulation transfer function (visited 17.05.2019).
URL https://www.edmundoptics.com/resources/application-notes/optics/introduction-to-modulation-transfer-function

[24] E. P. Goodwin, J. C. Wyant, Field Guide to Interferometric Optical Testing, SPIE, 2006.

[25] Scientific cmos technology - a high-performance imaging breakthrough, Tech. rep., Andor Technolgy, Fairchild Imaging, PCO Imaging (Jun. 2009).
URL http://ridl.cfd.rit.edu/products/sCMOS/scmos_white_paper_8mb.pdf

[26] Standard for characterization of image sensors and cameras release 3.1, Tech. rep., European Machine Vision Association (Dec. 2016).

[27] NASA Earth Observatory, Normalized Difference Vegetation Index (NDVI) (visited 18.05.2019).
URL https://earthobservatory.nasa.gov/features/MeasuringVegetation/measuring_vegetation_2.php

[28] United Nations Office for Outer Space Affairs, Top of the atmosphere(TOA) (visited 18.05.2019).
URL http://www.un-spider.org/node/10958

[29] ECSS system - Glossary of terms (ECSS-S-ST-00-01C), Tech. rep., European Cooperation for Space Standardization (Oct. 2012).

[30] D. Liltwiller, Ccd vs. cmos: Facts and fiction.

[31] J. R. Miller, E. W. Hare, J. Wu, Quantitative characterization of the vegetation red edge reflectance 1. an inverted-gaussian reflectance model, International Journal of Remote Sensing 11 (10) (1990) 1755–1773. doi:10.1080/01431169008955128.

[32] I. Lindseth, A. Bardal, R. Spooren, Reflectance measurements of aluminium surfaces using integrating spheres, Optics and Lasers in Engineering 32 (5) (1999) 419 – 435. doi:https://doi.org/10.1016/S0143-8166(00)00010-5.

[33] Rocky Mountain Institute Co., Enhanced aluminium coating (visited 16.05.2019).
URL http://rmico.com/enhanced-aluminum

[34] Semrock, 765 nm edge brightline single-edge image-splitting dichroic beamsplitter (visited 16.05.2019).
URL https://www.semrock.com/FilterDetails.aspx?id=FF765-Di01-25x36x2.0

[35] Semrock, 660/30 nm brightline single-band bandpass filter (visited 16.05.2019).
URL https://www.semrock.com/FilterDetails.aspx?id=FF01-660/30-25

[36] Semrock, 857/30 nm brightline single-band bandpass filter (visited 16.05.2019).
URL https://www.semrock.com/FilterDetails.aspx?id=FF01-857/30-25

[37] Schott, Radhard glass SF6G05 (1 2014).

[38] D. Korsch, Reflective Optics, Elsevier, Burlington, MA, USA, 1991.

[39] R. Geyl, Design and fabrication of a three-mirror, flat-field anastigmat for high-resolution earth observation, Space Optics 1994: Space Instrumentation and Spacecraft Optics 2210. doi:https://doi.org/10.1117/12.188135.

[40] K. Dohlen, M. Saisse, G. Claeysen, P. L. Lamy, J.-L. Boit, Optical designs for the rosetta narrow-angle camera, Optical Engineering 35 (4). doi:https://doi.org/10.1117/1.600710.

[41] ESA, Sentinel-2 MSI performance (visited 16.05.2019).
URL https://earth.esa.int/web/sentinel/technical-guides/sentinel-2-msi/performance/

[42] Andover Corporation, Bandpass filter fundamentals (visited 20.05.2019).
URL https://www.andovercorp.com/technical/bandpass-filter-fundamentals/

Appendix

Band= 645-675 nm, h=1000km					
D= 1,88 cm, integ. time=4ms			input	output	unit
Optics trans. factor = 0,78					
	Abreviation	Formula			
λ start			645		nm
λ end			675		nm
bandwidth				30	nm
λ center				660	nm
solar power density in this bandwitdh	E_λ	=integral over the bandwidth		51,75	Watt/m2
Assumed surface reflectance	ρ		0,05		[1]
Surface radiance (Lambertian)	L_λ	=ρ · E_λ / π	0	0,82	W/(m2*str)
Focal length	f		13,05		cm
Lens/aperture diameter	D		1,88		cm
Pixel pitch	Γ		6,5		µm
Number of detectors	N		1		[1]
Satellite height	h		1000		km
Max distance to targer (includes off-nadir ar	r		1000		
Ground sample distance (at nadir)	GSD	GSD=h * Γ / f		49,8	m
Ground sample distance (off-nadir)				49,8	m
Diffraction limit factor	Q	Q= Γ / (2.44 λ / D*f)		0,6	[1]
Pixel radiant intensity	I_λ	=L_λ ·(GSD)^2		2043,32	W/str
Atmopshere transmission [%] (assumed)	τ			73,40	[%]
Satellite velocity	Vs			7,35	km/s
Period	T			105,1	min
Ground track velocity	Vg	Vg=2pi*Re/T		6,35	km/s
Solid angle	Ω	=pi/(h^2)*(D/2)^2		3,53E-16	rad
Optics transmission factor (BOL=0.783, EOL	τ_optics		0,78		[1]
Power available before CCD	P_CCD			4,13E-13	W
Dwell tiime	T_dwell	GSD/Vg		7,84	ms
Integration time (<= dwell time)	T_integration		4,00		ms
Ground resolution (include smearing) at NADIR				75,22	m
Energy available	E_CCD	=Pr*T_integration	c a	1,65E-15	Joule=Ws
Energy of one photon at center of the band (660 nm)		=h*f=h*c0 / λ		3,01E-19	Joule=Ws
Number of available photons	Np			5495	photons
Quantum efficiency of sensor [%] at 660 nm				89,13	%
Number of electrons at reflectance = 0,05				4898	electrons
Number of electrons at reflectance = 1				58774	electrons
Total number of electrons	Ne			4898	electrons
Noise electrons	σ_n	=sqrt(Ne)		70	electrons
Read-out noise electrons	σ_ro		1,6		electrons
SNR of image	Ne/SQRT(σ_n^2+σ_ro^2)			70	[1]
Dymanic range of sensor at reflectance = 0,	DR			3061	11,6
Dymanic range of sensor at reflectance = 1	DR			61223	15,9

Figure 5.1: The unedited version of the radiometric budget for the 660(30) nm band from the radiometric budget worksheet

Band= 842-872 nm, h=1000km					
D= 1,88 cm, integ. time=4ms			input	output	unit
Optics trans. factor = 0,78					
	Abreviation	Formula			
λ start			842		nm
λ end			872		nm
bandwidth				30	nm
λ center				857	nm
solar power density in this bandwitdh	E_λ	=integral over the bandwidth		35,85	Watt/m2
Assumed surface reflectance	ρ		0,36		[1]
Surface radiance (Lambertian)	L_λ	=ρ · E_λ / π	0	4,11	W/(m2*str)
Focal length	f		13,05		cm
Lens/aperture diameter	D		1,88		cm
Pixel pitch	Γ		6,5		µm
Number of detectors	N		1		[1]
Satellite height	h		1000		km
Max distance to targer (includes off-nadir an	r		1000		
Ground sample distance (at nadir)	GSD	GSD=h * Γ / f		49,8	m
Ground sample distance (off-nadir)				49,8	m
Diffraction limit factor	Q	Q= Γ / (2.44 λ / D*f)		0,4	[1]
Pixel radiant intensity	I_λ	=L_λ ·(GSD)^2		10191,72	W/str
Atmopshere transmission [%] (assumed)	τ			72,33	[%]
Satellite velocity	Vs			7,35	km/s
Period	T			105,1	min
Ground track velocity	Vg	Vg=2pi*Re/T		6,35	km/s
Solid angle	Ω	=pi/(h^2)*(D/2)^2		3,53E-16	rad
Optics transmission factor (BOL=0.783, EOL	τ_optics		0,78		[1]
Power available before CCD	P_CCD			2,03E-12	W
Dwell tiime	T_dwell	GSD/Vg		7,84	ms
Integration time (<= dwell time)	T_integration		4,00		ms
Ground resolution (include smearing) at NADIR				75,22	m
Energy available	E_CCD	=Pr*T_integration	c a	8,13E-15	Joule=Ws
Energy of one photon at center of the band (857 nm)		=h*f=h*c0 / λ		2,32E-19	Joule=Ws
Number of available photons	Np			35071	photons
Quantum efficiency of sensor [%] at 857 nm				53,23	%
Number of electrons at reflectance = 0,36				18666	electrons
Number of electrons at reflectance = 1				31111	electrons
Total number of electrons	Ne			18666	electrons
Noise electrons	σ_n	=sqrt(Ne)		137	electrons
Read-out noise electrons	σ_ro		1,6		electrons
SNR of image	Ne/SQRT(σ_n^2+σ_ro^2)			137	[1]
Dymanic range of sensor at reflectance = 0,	DR			11666	13,5
Dymanic range of sensor at reflectance = 1	DR			32407	15,0

Figure 5.2: The unedited version of the radiometric budget for the 857(30) nm band from the radiometric budget worksheet

Lihtlitsents lõputöö reprodutseerimiseks ja üldsusele kättesaadavaks tegemiseks

Mina, Joosep Kivastik,

1. annan Tartu Ülikoolile tasuta loa (lihtlitsentsi) minu loodud teose

   "Radiomeetriliselt kalibreeritud miniatuurse maavaatluskaamera optiline ülesehitus"

   mille juhendajad on Hendrik Ehrpais ja Nikolay Voznesenskiy,

   reprodutseerimiseks eesmärgiga seda säilitada, sealhulgas lisada digitaalarhiivi DSpace kuni autoriõiguse kehtivuse lõppemiseni.

2. Annan Tartu Ülikoolile loa teha punktis 1 nimetatud teos üldsusele kättesaadavaks Tartu Ülikooli veebikeskkonna, sealhulgas digitaalarhiivi DSpace kaudu Creative Commonsi litsentsiga CC BY NC ND 3.0, mis lubab autorile viidates teost reprodutseerida, levitada ja üldsusele suunata ning keelab luua tuletatud teost ja kasutada teost ärieesmärgil, kuni autoriõiguse kehtivuse lõppemiseni.

3. Olen teadlik, et punktides 1 ja 2 nimetatud õigused jäävad alles ka autorile.

4. Kinnitan, et lihtlitsentsi andmisega ei riku ma teiste isikute intellektuaalomandi ega isikuandmete kaitse õigusaktidest tulenevaid õigusi.

Joosep Kivastik
03.06.2019